Measurement and analysis of energy and angular distributions of thick target neutron yields from 110 MeV ^{19}F on ^{27}Al

Sunil C[*]
Accelerator Radiation Safety Section, RSSD, Bhabha Atomic Research Centre, Mumbai 400085, India

Maitreyee Nandy[†]
Saha Institute of Nuclear Physics, 1/AF, Bidhannagar, Kolkata 700064, India

P. K. Sarkar[‡]
H.P. Unit (RSSD, BARC), Variable Energy Cyclotron Centre, 1/AF, Bidhannagar, Kolkata 700064, India
(Received 13 August 2008; published 10 December 2008)

Energy distributions of emitted neutrons were measured for 110 MeV ^{19}F ions incident on a thick ^{27}Al target. Measurements were done at 0°, 30°, 60°, 90°, and 120° with respect to the projectile direction employing the time-of-flight technique using a proton recoil scintillation detector. Comparison with calculated results from equilibrium nuclear reaction model codes like PACE-2 and EMPIRE 2.18 using various level-density options was carried out. It is observed that the dynamic level-density approach in EMPIRE 2.18 gives the closest approximation to the measured data. In the Fermi-gas level-density approach the best approximation of the level-density parameter is $a = A/12.0$, where A is the mass number of the composite system. The trend in the angular distribution of emitted neutrons is well reproduced by the projection of the angular momentum on the recoil axis as done in the PACE-2 code.

DOI: 10.1103/PhysRevC.78.064607 PACS number(s): 24.10.−i, 29.30.Hs, 25.70.−z

I. INTRODUCTION

Neutron emissions from thick targets are important in a positive ion accelerator facility, as these neutrons are the major constituents of prompt radiation environment in the case of beam loss during normal operations or accidental situations. The neutron dose is a function of the energy distribution of emitted neutrons, which in an accelerator environment varies depending on the projectile, target, and incident energy. Low-energy heavy-ion beams are in widespread use for nuclear and atomic studies, for surface analysis, and atomic mass spectrometry and in industry for material modification and semiconductor production. Some of these beams have the potential to produce radiation, principally fast neutrons that are harmful to people or damaging to sensitive detectors or other delicate equipment. The neutron yield and energy distributions are important parameters in neutron dosimetry and shielding studies of heavy-ion accelerators. Data on the energy-angular distribution of secondary neutrons from a thick target, which fully stops heavy ions, called the thick target neutron yield (TTNY), are essential to estimate source terms of the accelerator shielding design. Such data are also useful to calculate the dose delivered to the patient by secondary neutron interactions during heavy-ion irradiation. Furthermore, these data are expected to provide some insight into the nature of the neutron spectra produced by interactions of heavy ions present in galactic cosmic rays with shielding materials [1] used to protect humans engaged in long-term missions outside the geomagnetosphere.

Measurement of the energy distributions of TTNY at different angles with respect to the incident beam direction is more important for radiation protection purposes compared to direct measurement of dose equivalent quantities. This is because the dose equivalent is a quantity estimated from the neutron energy distribution through fluence to dose conversion coefficients, which can be, and have been, changed by the International Commission on Radiological Protection (ICRP). However, neutron energy spectra remain invariant and can be used to compute the dose equivalent in the case of any future change in fluence to dose conversion coefficients, whereas the reverse is not possible.

In the case of light ion projectiles such as protons and α particles, TTNY has been measured by several workers [2–5]. But in the case of heavy-ion projectiles such data are few and, even among those, only three or four measurements are in the projectile energy range of 10 MeV/nucleon or less [6–9]. However, heavy-ion accelerators in this energy range are employed in significant numbers for different applications including basic research.

Computation of neutron energy spectra and their angular distributions by various nuclear reaction model codes are also practiced for accelerator radiation protection calculations in the absence of measured data. It is imperative to know how well these calculations compare with the experimental measurements. If such data are used without validation large errors can occur in radiological safety design.

Additionally, an analysis of TTNY gives insights of the reaction mechanisms involved [3,8,10,11], even though the emitted spectrum from a thick target is a superposition of

[*]sunilc@barc.gov.in
[†]mnandy@hp2.saha.ernet.in
[‡]Corresponding author: pks@veccal.ernet.in

spectra from different stages of a continuously degrading projectile energy. The thickness of the target can be so chosen that the projectile is completely stopped inside it. Thus it becomes feasible to make measurements at extreme forward angles with respect to the incident projectile direction. For historical reasons, the reactions induced by light ions are generally well known, including those that lead to neutrons in the exit channel. In contrast, the production of neutrons by heavy-ion reactions is not well understood. The use of heavy ions allows one to study compound-nuclear reactions at high excitations and high values of angular momentum. For protons and other light projectiles with energies around 100 MeV the emitted spectra can be described in part by mechanisms involving few nucleon-nucleon interactions in the initial phase. For heavy ions, however, the initial energy is shared by many nucleons and the few nucleon effects are thus expected to be small (at least for projectiles with energies around 6*A* MeV). The entire de-excitation process is supposed to be adequately described by the statistical model in this case. It is therefore expected that the heavy-ion-induced reactions will allow a more simple and unambiguous test of the compound-statistical model at high excitation energies. In an earlier work [8], we observed slight pre-equilibrium neutron emission from 7.2 *A* MeV ^{16}O on ^{181}Ta. It would be interesting to see whether any such pre-equilibrium emissions take place at about 5.8 *A* MeV ^{19}F on ^{27}Al. Moreover, with heavy ions as projectiles, the amount of orbital angular momentum brought in far exceeds the usual nuclear spins, causing the resulting compound nucleus to be highly spin aligned. This is expected to have a significant effect on the angular distribution of emitted particles, which will be interesting to study.

We measured neutron yield distributions from 110 MeV ^{19}F projectiles on a thick ^{27}Al target at 0°, 30°, 60°, 90°, and 120° with respect to the projectile beam direction using the time-of-flight (TOF) technique. The main purpose of these measurements is to investigate the compound nuclear neutron emission from such high excitation energy at which the preequilibrium (PEQ) emission remains negligibly small. We analyzed the measured data using two well-known nuclear reaction model codes, namely EMPIRE 2.18 [12] and PACE-2 [13]. We intend to test and compare these codes and different level-density options at projectile energies around the threshold of PEQ emissions.

In Sec. II we describe our measurement procedure and data unfolding technique. Section III gives the procedure adopted to calculate thick target neutron yield distributions and in Sec. IV a brief outline of the codes used for the calculations is given. We present our experimental and theoretical results and discuss them in Sec. V.

II. EXPERIMENTAL PROCEDURE

The experiment was conducted at the BARC-TIFR Pelletron Accelerator Facility located in Mumbai, India. A thick target of Al, 2 mm thick and 45 mm in diameter, was mounted inside a small chamber of about 1 mm wall thickness. The arrangement was electrically isolated from the rest of the beam line using an insulator and a 30-cm-long SS tube. This had the effect of electron suppression, as the electrons escaping from the target were collected within the electrically isolated arrangement thereby ensuring accurate beam current measurement. BC501 liquid scintillator detectors were kept at a distance of 1.5 m from the target at 0°, 30°, 60°, and 90° with respect to the beam direction. For 120° the detector was kept at a distance of 1.0 m. The angles of acceptance of the detector for such arrangements are ±0.96° for angles 0°–90° and ±1.43° for 120°. Because BC501 detector is sensitive to γ photons, we used a standard pulse-shape discrimination technique [14] to distinguish neutrons from photons. The neutron energy was determined by the TOF technique. The anode output from the PMT was amplified and used as the energy-dependent pulse height data (first parameter). The dynode output from the PMT was used for pulse shape (PS) discrimination (second parameter) and as a start signal for the TOF (third parameter). The radio frequency signal from the beam buncher was used as the stop signal for the TOF. All three parameters were acquired by a multiparameter data acquisition system in list mode for off-line analysis. Using the TOF and PS parameters the neutrons were separated off-line from the γ photons using a proper software gate. Using this technique it was possible to extract neutron pulses as low as 0.5 MeV.

In Fig. 1 we give a scatter plot of the pulses obtained from the BC501 scintillator placed at 120° with respect to the projectile direction. Each point in the diagram represents a pulse from the detector. These pulses are analyzed and binned (vertical direction) as per their zero crossover time in the pulse-shape discriminator (PSD) and as per their flight time (horizontal direction) from the target to the detector. The horizontal axis is marked with neutron energy corresponding to the flight time for convenience in representation. This energy scale does not represent γ energies for the γ pulses. The horizontal scale is nonlinear because flight time and particle energy has a nonlinear relationship. The zero crossover time is smaller for pulses due to γs compared to those due to

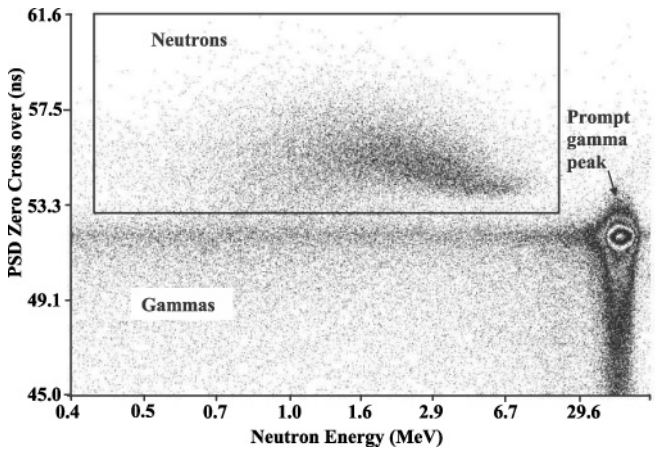

FIG. 1. Two-dimensional scatter diagram of zero cross-over time of the detector pulses in the pulse shape discriminator (PSD) plotted against flight time converted to neutron energy. The plot is generated from the measured pulse heights from the BC501 scintillation detector placed at 120°. The points within the rectangular box correspond to the pulses due to neutrons.

neutrons and thus can be separated. The pulses within the rectangular box are due to neutrons. These pulses are extracted and analyzed to obtain the neutron energy distribution. The left vertical side of the box corresponds to neutron energy of about 0.43 MeV, whereas the right side corresponds to about 20 MeV of neutron energy. Because our energy bin is 0.5 MeV wide any neutron pulse having energy between 0 and 0.5 MeV are accumulated in the 0.5-MeV bin. A cluster of pulses corresponding to the prompt γ peak is marked in the figure, which helps in calibrating the system. The horizontal band appearing in the plot just below the rectangular box is due to γs with delayed emission or due to γs scattered back into the detector from the surrounding materials or both.

The efficiency of the detector was estimated using Monte Carlo simulations, which consider cut-off of electronic pulses up to a certain amplitude (corresponds to about 80 keV of photon energy) to eliminate noise. Time calibration of the detector system was done by introducing known delays and measuring channel shifts in the prompt γ pulse from the target while the beam is incident on it. Off-line calibration was also done by feeding pulses at different intervals from a precision pulse generator. Because the measurements are inclusive, neutrons scattered from the wall and other structures add to the energy spectrum from direct neutrons. To eliminate this contribution, each set of measurement was repeated by blocking the line of sight of the detector from the target by means of 30.0-cm iron followed by 30.0-cm paraffin bars. This arrangement allows counting of only those neutrons that get scattered form the surrounding materials. The true spectrum is then obtained by subtracting the scattered component.

A. Uncertainties in measurement

Errors or uncertainties in the measurements with the TOF technique employing BC501 arise due to different factors, including the uncertainty in overall beam current normalization, which is estimated to be about 2%. For the TOF technique the sources of error are mainly due to factors affecting the time resolution and consequently the energy resolution. The relative energy resolution is given by:

$$\frac{\Delta E}{E} = \gamma(\gamma+1)\left(\frac{\Delta t}{t}\right), \tag{1}$$

where $\gamma = 1 + \frac{E}{Mc^2}$

Here, E is the neutron kinetic energy, M the neutron rest mass, Δt the overall time resolution, and t the neutron flight time. When factors like time dispersions due to beam energy spread and finite thickness of the target are ignored as negligible, the major contributing factors to Δt are as follows: (i) the time spread of the beam pulse (2.5 ns), (ii) intrinsic time resolution of the neutron detector (about 2 ns), and (iii) the time spread resulting from the finite thickness (5.0 cm) of the detector. Considering these three factors the estimated energy resolution ($\Delta E/E$) for the 1.5-m flight path is about 8% at 1 MeV, about 16% at 10 MeV, and about 25% at 25 MeV.

There will be uncertainties in the energy distribution due to the combined time dispersion discussed above. Assuming the uncertainty in energy E to have a Gaussian distribution centered around E with full width at half maximum equal to ΔE, we can correct for the loss of resolution in the measured data as follows.

If $\phi(E)$ is the the true energy distribution of neutrons, which is smeared by the Gaussisn functions to give the observed distribution $\phi^{\text{obs}}(E)$, then

$$\phi^{\text{obs}}(E) = \int_0^{E_{\max}} R(\acute{E}, E)\phi(\acute{E})d\acute{E}, \tag{2}$$

where

$$R(\acute{E}, E) = \frac{1}{C}\exp\left[\frac{-(\acute{E}-E)^2}{2\sigma_R^2}\right]$$

such that

$$\int_0^{E_{\max}} \frac{1}{C}\exp\left[\frac{-(\acute{E}-E)^2}{2\sigma_R^2}\right]d\acute{E} = 1.$$

Here, $\sigma_R = \Delta E/2.355$ and $E_{\max}$ is the maximum energy of the observed distribution.

For numerical work Eq. (2) can be transformed approximately into the discretized linear matrix equation

$$\mathbf{\Phi^{obs}} = \mathbf{R\Phi}. \tag{3}$$

Here the response matrix $\mathbf{R}$ has elements R_{ij} that indicates the contribution from the discretized energy channel j to the energy channel i because of the Gaussian smearing.

The evaluation of the true distribution $\mathbf{\Phi}$ from the relation as expressed in Eq. (3) is known as unfolding or solving the inverse problem of spectrometry. There are many suggested techniques that can be adopted for such unfolding [15]. However, because of the errors associated with $\mathbf{\Phi^{obs}}$ and for other reasons, many of these procedures are fraught with difficulties. In the present work, we adopted a relatively simple one [15] based on iterative improvement of the solution where $(k+1)$-th solution $\phi_j^{(k+1)}$ is obtained from the (k)-th iterative solution $\phi_j^{(k)}$ as

$$\phi_j^{(k+1)} = \phi_j^{(k)}\left[\sum_i \frac{\phi_i^{\text{obs}} D_{ij}}{\sum_j R_{ij}\phi_j^{(k)}}\right] \Bigg/ \sum_i D_{ij} \tag{4}$$

$$D_{ij} = \frac{R_{ij}}{\phi_i^{\text{obs}}}\frac{1}{\rho_i^2}, \tag{5}$$

where ρ_i is the standard deviation of the error associated with the measured data ϕ_i^{obs}. As is evident, an initial guess distribution $\phi_j^{(0)}$ has to supplied for this procedure to work. We considered $\phi_j^{(0)} = \phi_j^{\text{obs}}$ for the present work. We terminated the iteration when the difference between $\phi_j^{(k+1)}$ and $\phi_j^{(k)}$ is less than or equal to 0.01%.

The total error associated with the unfolded spectra consists of (i) the statistical error associated with the measurement, (ii) the error arising from discretizing the continuous spectra and the response function, and (iii) the error associated with the response matrix. We considered only the statistical error associated with the measurement and ignored the other two types of error because they are comparatively of smaller

magnitude. We also ensured that the number of counts in the measured and the unfolded data is same.

III. ESTIMATION OF THICK TARGET NEUTRON YIELD DISTRIBUTION

In a thick target, the projectile interacts with the target nuclei at different continuously degrading energies and the observed emitted spectrum is a sum of emissions from all these projectile energies within the target. For ease of calculations we divided the thick target into a number of thin slabs such that the projectile loses a specified energy ΔE in each slab. The projectile is assumed to interact with all target nuclei in its path within this thin slab with an average energy. The slowing down is thus considered in small discrete steps. The emitted spectra from all of these slabs are summed up to give the final spectra. While considering the continuous slowing down of the projectile we ignored multiple scattering and straggling of the projectile in the target [3]. The change in neutron energy distributions due to scattering of the emitted neutrons in the target was found negligible at all angles except at 90° where a slight change was observed [16]. The experimental data presented in this article are corrected accordingly. The kinetic energy E_P^i incident on the i-th slab and the average energy in the i-th slab $\bar{E}_P^i$ are given, for a projectile of energy E_P^0 incident on the thick target, by

$$\begin{aligned} E_P^i &= E_P^0 - (i-1)\Delta E \\ \bar{E}_P^i &= \left(E_P^i + E_P^{i+1}\right)/2. \end{aligned} \tag{6}$$

The slab thickness x_i is

$$x_i = \int_{E_P^i}^{E_P^{i+1}} \frac{dE}{-dE/dx}, \tag{7}$$

where dE/dx is the stopping power of the projectile in the target material that was calculated using the formalism of Ziegler *et al*. [17].

The neutron yield $\phi(\epsilon,\theta)d\epsilon d\theta$ at energy ϵ and direction θ with respect to the initial projectile direction is given by

$$\begin{aligned} \phi(\epsilon,\theta)d\epsilon d\theta = &\sum_{i=1}^{m} \sigma\left(\bar{E}_P^i;\epsilon,\theta\right)d\epsilon d\theta a_n x_i \\ &\times \exp\left\{-a_n\left[\sum_{k=1}^{i-1}\sigma_{\text{fus}}\left(\bar{E}_P^k\right)x_k\right]\right\}, \end{aligned} \tag{8}$$

where a_n is the number of target atoms per unit volume, $m = (E_P^0 - E_P^{\text{th}})/\Delta E$, E_P^{th} being the projectile threshold energy for neutron production. For $i = 1$ the value of the exponential attenuation factor in Eq. (8) is taken to be unity. $\sigma(E_P;\epsilon,\theta)$ is the emission cross section of neutrons of energy ϵ at an angle θ when a projectile of energy E_P is incident on a target nucleus. Here, σ_{fus} is the fusion cross section of the projectile with the target.

IV. NUCLEAR REACTION MODELS AND COMPUTER CODES USED

A. PACE

PACE is described as the projection angular-momentum coupled evaporation code [13] where the de-excitation of the excited nucleus is calculated by coupling angular momenta at each stage of de-excitation using a Monte Carlo simulation by choosing randomly different channels. This is done after the initial spin distribution (normalized to unity) of the starting excited nucleus is calculated. The determination of the probabilities of the path of de-excitation is carried out by using random numbers to establish different decay channels of the compound nucleus. Thus all possible decay channels are considered randomly according to their respective probabilities. Transmission coefficients for light particle (n, p, α) evaporation are obtained by optical model calculations. A fission decay mode is incorporated using rotating liquid drop fission barrier. Angular momentum projections are calculated at each stage of de-excitation to determine the angular distribution of emitted particles as functions of angle around the recoil axis. Fusion cross sections are calculated using the model proposed by Bass [18]. The level-density formulation used for excitation energy U and angular momentum J is

$$\rho(U,J) = \frac{2J+1}{2\sqrt{2\pi}\sigma^3}\rho(U)\exp\left[-\frac{(J+0.5)^2}{2\sigma^2}\right], \tag{9}$$

where

$$\rho(U) = \frac{\sqrt{\pi}}{12a^{1/4}U^{5/4}}\exp[2\sqrt{aU}]. \tag{10}$$

Here, a is the level-density parameter and σ^2 is the spin cut-off parameter.

B. EMPIRE 2.18

EMPIRE is a modular system of nuclear reaction codes [12], comprising various nuclear reaction models and designed for calculations over a broad range of energies and incident particles. A projectile can be a neutron, proton, any ion (including heavy ions), or a photon. The energy range extends from a few keV for neutron-induced reactions and goes up to several hundreds of MeV for heavy-ion-induced reactions. The code accounts for the major nuclear reaction mechanisms, including direct, pre-equilibrium, and compound nuclear ones. The compound nucleus decay is described by the Hauser-Feshbach model with γ-cascade and width fluctuations. Treatment of the fission channel takes into account transmission through a multiple-humped fission barrier with absorption in the wells. The fission probability is derived in the Wentzel-Kramers-Brillouin approximation within the optical model of fission. The statistical model used in EMPIRE is an advanced implementation of the Hauser-Feshbach theory. The exact angular momentum and parity coupling is observed using l-dependent transmission coefficients. The emission of neutrons, protons, α particles, and a light ion is taken into account along with the competing fission channel. Angular distributions of particles emitted from the compound nucleus

are assumed to be isotropic. The full γ cascade in the residual nuclei is considered.

Determination of the level densities can be carried out in the nonadiabatic approach allowing for the rotational and vibrational enhancements. These collective effects are gradually removed above a certain energy. Level densities acquire dynamic features through the dependence of the rotational enhancement on the shape of the nucleus. In the frame of the statistical model of nuclear reactions, the contribution of the compound nucleus (CN) state with certain spin, parity, and excitation energy to a channel is given by the ratio of the channel width to the total width multiplied by the population of this state. This also holds for secondary CNs that are formed due to subsequent particle emission. The only difference is that although the first CN is initially excited to the unique (incident channel compatible) energy, the secondary CNs are created with excitation energies that spread over the available energy interval. Each such state contributes to the cross section. The following assumptions are made in the course of these calculations: (i) particle emission from a nucleus at a certain excitation energy is independent of the actual recoil energy of the nucleus: the center of mass motion of a nucleus (recoil) is assumed to have no effect on the emission of particles, as the latter involves internal degrees of freedom. (ii) Compound nucleus emissions are isotropic and uncorrelated: EMPIRE accounts for various models describing level densities and includes several parametrizations of these.

1. EMPIRE*-specific level densities*

The dynamic approach to the level densities is specific to the EMPIRE code. It takes into account collective enhancements of the level densities due to nuclear vibration and rotation. The formalism uses the super-fluid model below a critical excitation energy and the Fermi gas model above. Differing from other similar formulations, the former accounts explicitly for the rotation-induced deformation of the nucleus, which becomes spin dependent. The deformation enters the level-density formula through the moments of inertia and through the level-density parameter a that increases with the increase of the surface of the nucleus.

EMPIRE-specific level densities, in addition to their explicit treatment of the collective effects and their damping, also include the effects of dynamical deformation, which is induced by the rotation of a nucleus at high spin. The yrast line is taken into account by setting level densities to zero whenever the thermal energy available for single-particle motion is negative. The thermal energy is calculated as the difference between the total excitation energy and the energy needed for rotation. Spin and energy ranges are also formally unlimited in the EMPIRE-specific level densities. These features make the approach particularly suited for heavy-ion and high-energy nucleon-induced reactions. However, EMPIRE-specific level densities are fitted to the experimental data in a manner similar to the Gilbert-Cameron (GC) formalism, suggesting that their predictions at low energies should be comparable to those of GC or even better due to the use of the BCS model below a critical energy. Therefore, EMPIRE-specific level densities are generally recommended and are used as a default in the EMPIRE code. However, EMPIRE-specific level densities suffer the same uncertainty as GC level densities when extrapolating from the stability line, because both rely on experimental parametrization of the level-density parameter a, which is possible only for stable or close to stable nuclei.

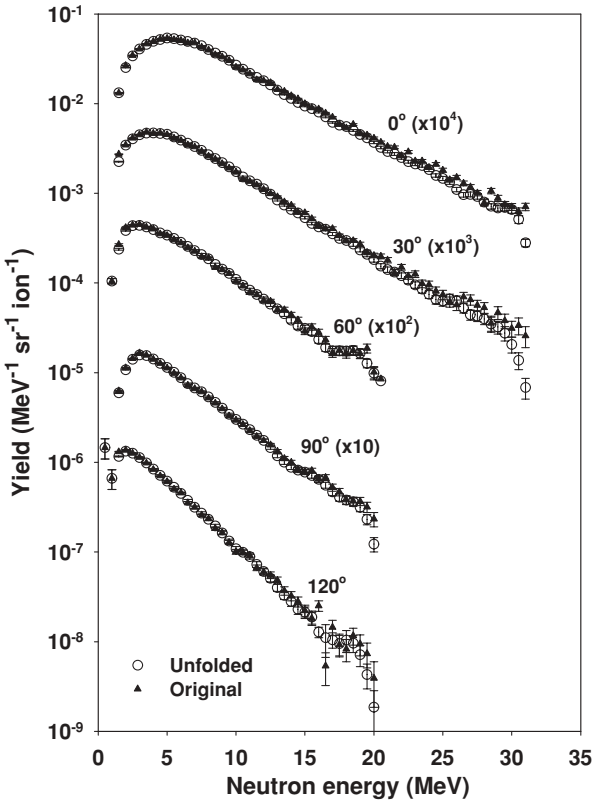

FIG. 2. Plots of experimental measurements and unfolded data for energy distributions of neutron yield from 110 MeV ^{19}F on a thick ^{27}Al target at 0°, 30°, 60°, 90°, and 120°. The data at different angles are multiplied with factors as indicated alongside the plots. The angles of acceptance of the detector are $\pm 0.96°$ for 0°–90°, and $\pm 1.43°$ for 120°.

V. RESULTS AND DISCUSSIONS

We corrected for the loss of resolution in the measured data using the unfolding procedure as outlined in Sec. II A. In Fig. 2 we plot the measured and the unfolded distributions at 0°, 30°, 60°, 90°, and 120° angles with respect to the incident ^{19}F beam direction. As can be observed, the unfolded distribution differs from the measured data only at high neutron emission energies. This is expected because the energy resolution of the TOF system becomes poorer with increasing neutron energy. In what follows, we present these unfolded data as experimental data unless mentioned otherwise.

In Fig. 3 we plot the unfolded energy distributions of neutrons (open circles with error bars) at 0°, 30°, 60°, 90°, and 120°. In the same figure also plotted are the calculated results using the codes EMPIRE 2.18 as solid lines and PACE-2 as broken lines. We can observe that PACE-2 results overestimate

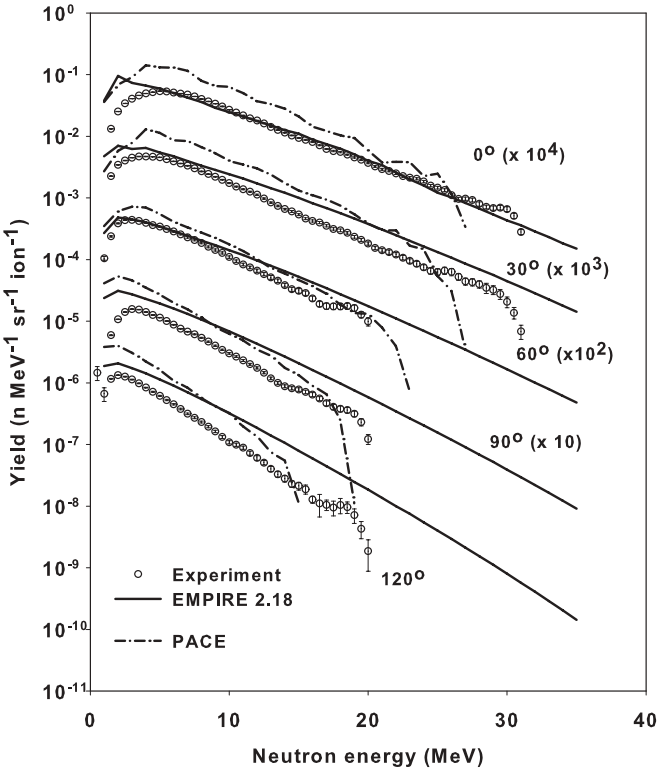

FIG. 3. Energy distributions of neutron yield from 110 MeV ^{19}F on a thick ^{27}Al target at 0°, 30°, 60°, 90°, and 120°. The data at different angles are multiplied with factors as indicated alongside the plots. The symbols with error bars represent measured (unfolded) data, the solid lines are calculated results from EMPIRE 2.18 using EMPIRE-specific dynamic level densities (default option), the dash-dots are results from PACE-2 with Fermi-gas level densities and $a = A/7.5$ (default option). For the experimental data the angles of acceptance of the detector are ±0.96° for 0°–90° and ±1.43° for 120°.

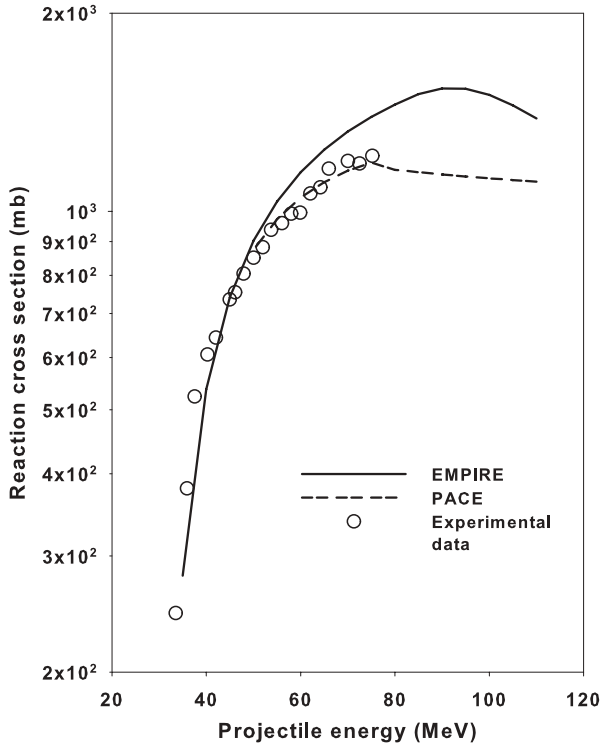

FIG. 4. Comparison of reaction cross section at different projectile energies for ^{19}F on ^{27}Al as calculated with the codes EMPIRE 2.18 (solid line) and PACE-2 (dash). The experimentally measured data [19] are plotted as symbols.

the measured distribution at all angles particularly at low energies (below about 15 MeV) and drop off suddenly at higher energies. The results from EMPIRE 2.18 match the experimental distribution well at 0° from 5 MeV upward, whereas at lower energies it overpredicts the experimental data. At 30° and 60° the EMPIRE 2.18 results overpredict the experimental data at high energies, whereas at 90° and 120° they grossly overpredict at all emission energies. At high energies and at forward angles there is no underprediction by EMPIRE 2.18 results that indicates the absence of pre-equilibrium emissions. It appears that EMPIRE 2.18 results do not reproduce the angular distribution of emitted neutrons correctly. In fact, EMPIRE 2.18 does not give any angular distribution; instead it gives the energy differential neutron emission cross section in the center-of-mass system. We converted the cross sections in the center-of-mass system to the laboratory system by assuming the emission to be isotropic in the cm system and thus adding the cm velocity to the velocity of the emitted neutrons. Once the double differential cross section is obtained they were converted to double differential neutron yield distributions $Y(\epsilon, \theta)$ following the procedure described in Sec. III. PACE-2, however, gives double differential neutron emission cross sections $\sigma(\epsilon, \theta)$ in the laboratory frame of reference. These cross sections at various degraded projectile energies were converted to double differential neutron yield distributions $Y(\epsilon, \theta)$.

The systematic overprediction at all angles by PACE-2 can be due to several reasons. One of the reasons may be overestimation of the reaction (fusion) cross section. We plotted in Fig. 4 the reaction cross section against projectile energy, where the solid line indicates the results from EMPIRE 2.18, the dotted line represents PACE-2 calculations, and the open circles are experimentally measured reaction cross sections of Chiou *et al.* as reported by Frobrich [19]. The experimental data are close to PACE-2 calculations. It is seen that EMPIRE 2.18 gives a higher fusion cross section above 50 MeV, whereas below that energy PACE and EMPIRE cross sections match and are represented by one solid line. It can also be seen that the experimental data closely matches the PACE-2 calculations. PACE-2 uses the Bass model to calculate the reaction cross section, whereas in EMPIRE 2.18 simplified coupled-channels approaches are used. It appears that for the present target and projectile system the Bass model yields reaction cross sections closer to the reported experimental data. We therefore used PACE-2-calculated reaction cross sections as input to EMPIRE 2.18 and plotted the calculated neutron yield distributions obtained from EMPIRE 2.18 in Fig. 5. In the figure the long dashes indicate the EMPIRE 2.18 results with PACE-2 calculated reaction cross sections while the solid line indicates the original results, and the symbols are the experimental data from the present work. It is observed, as expected, that the

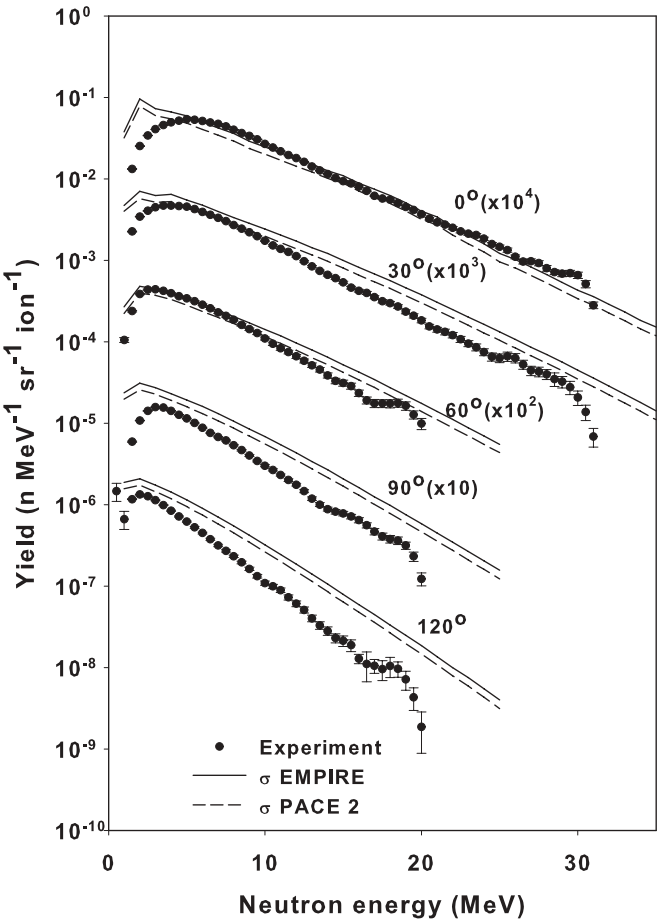

FIG. 5. Energy distributions of neutron yield from 110 MeV ^{19}F on a thick ^{27}Al target at 0°, 30°, 60°, 90°, and 120°. The data at different angles are multiplied with factors as indicated alongside the plots. The symbols with error bars represent measured (unfolded) data, the solid lines are calculated results from EMPIRE 2.18 using EMPIRE calculated reaction cross sections (default option), while the long dashes are results from EMPIRE but using PACE-2 reaction cross sections.

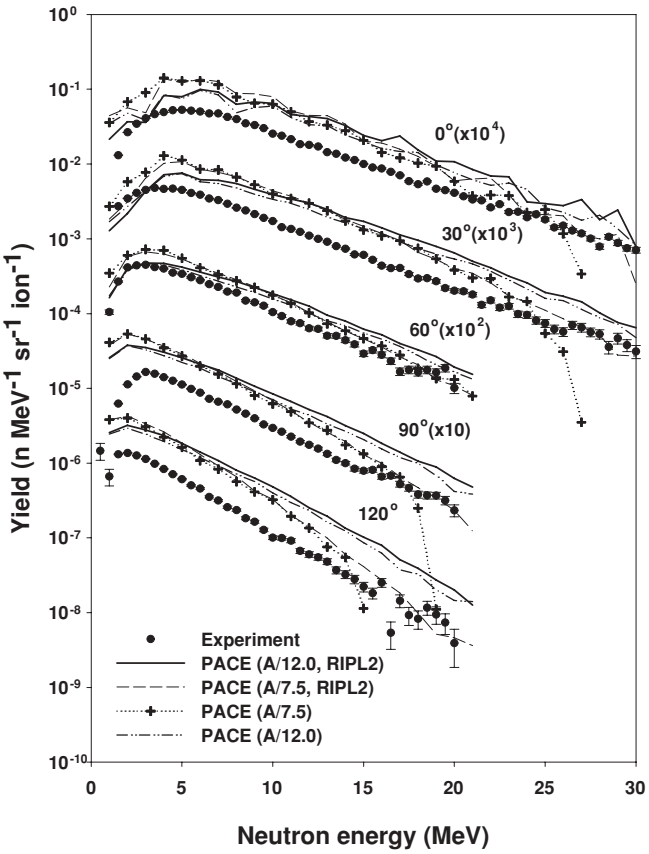

FIG. 6. Calculated (PACE-2) energy distributions of neutron yield from 110 MeV ^{19}F on a thick ^{27}Al target at 0°, 30°, 60°, 90°, and 120°. The data at different angles are multiplied with factors as indicated alongside the plots. The closed circles represent measured (unfolded) data, the solid and dashed lines are calculated results from PACE-2 with RIPL-2 optical model parameters, and the "plus" joined by dots and dash-double dots are with PACE-2 default optical model parameters.

results with the altered reaction cross sections are slightly less than the original results of EMPIRE 2.18, which makes the estimated yield distributions at larger angles closer to the experimental data. These results, however, do not resolve the problem of overprediction by PACE-2 at all angles.

Next, we investigate the optical model parameters that are used to calculate the emission cross section of various ejectiles in the two codes. PACE-2 has built-in default global parameters that are used while EMPIRE 2.18 uses the compiled RIPL-2 [20] optical model data library. We used in PACE-2 the optical model parameters from EMPIRE 2.18 and repeated the calculations. In Fig. 6 we compared the calculated results using PACE-2 with its default optical model parameters and those using the RIPL-2 data along with the experimental neutron yield. It can be observed that the change in the neutron emission is insignificant except at the highest energies for 90° and 120°. This is expected as the PACE-2 built-in optical model parameters are not very different from the RIPL-2 data.

Next, we investigate the effect of level-density options on the differential neutron yield and whether it can account for the overpredictions by PACE-2. To do this we consider the angle integrated energy differential neutron yield distributions (plotted in Fig. 7) obtained from experimental data (open squares with error bars), EMPIRE 2.18 results (lines) and the PACE-2 (symbols) results. As mentioned earlier we plotted in Fig. 3 the data obtained with the EMPIRE-specific dynamic approach level density that is plotted in Fig. 7 as a solid line. We also used the Fermi-gas level-density option in EMPIRE 2.18 with values of the 'a' parameter (in MeV^{-1}) as $A/7.5$ (dotted lines), $A/9.0$ (dash), and $A/12.0$ (dash with double dots). Similarly for PACE-2, the values of the 'a' parameter were chosen as $A/7.5$ (solid circles), which is the default option, along with $A/9.0$ (open circles) and $A/12.0$ (inverted solid triangles). It can be seen that the EMPIRE default option results overestimate the experimental distributions but the overestimation is much more for the PACE-2 default option particularly at low energies. It is also observed that results of EMPIRE 2.18 with Fermi-gas level-density option where $a = A/12.0$ is very close to the results obtained with the default option for the level density. The

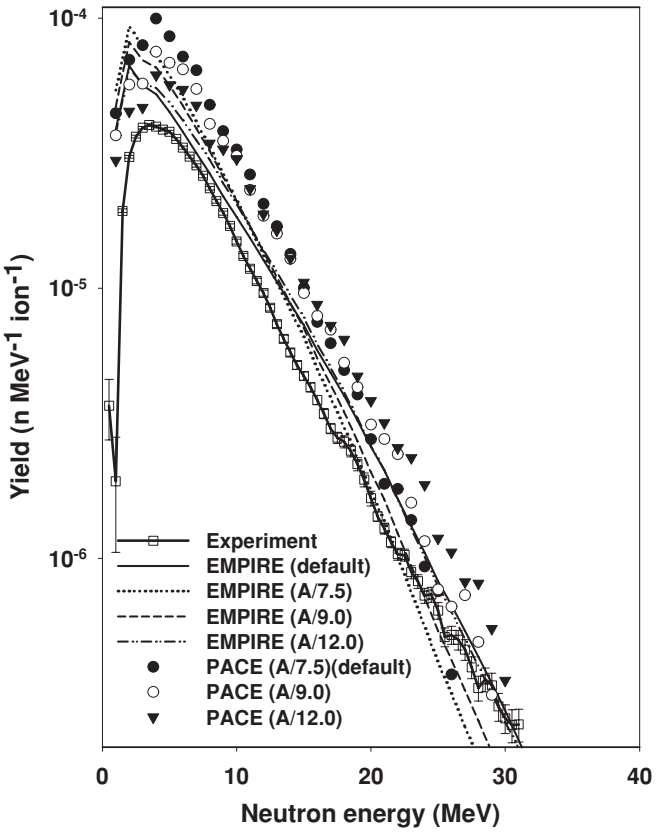

FIG. 7. Angle-integrated energy distributions of neutron yield from 110 MeV ^{19}F on a thick ^{27}Al target. Open squares with a line through them represent measured (unfolded) data. EMPIRE 2.18 results with different level-density option are plotted (i) as solid lines for EMPIRE-specific dynamic level densities (default option), (ii) as dots for the Fermi-gas level density (FGLD) with $a = A/7.5$ (MeV^{-1}), (iii) as dash for FGLD with $a = A/9.0$ (MeV^{-1}), (iv) as dash with two dots for FGLD with $a = A/12.0$ (MeV^{-1}). PACE-2 results are plotted (v) as solid circles for FGLD with $a = A/7.5$ (MeV^{-1}) (default option), (vi) as open circles for FGLD with $a = A/9.0$ (MeV^{-1}), and (vii) as solid inverted triangles for FGLD with $a = A/12.0$ (MeV^{-1}).

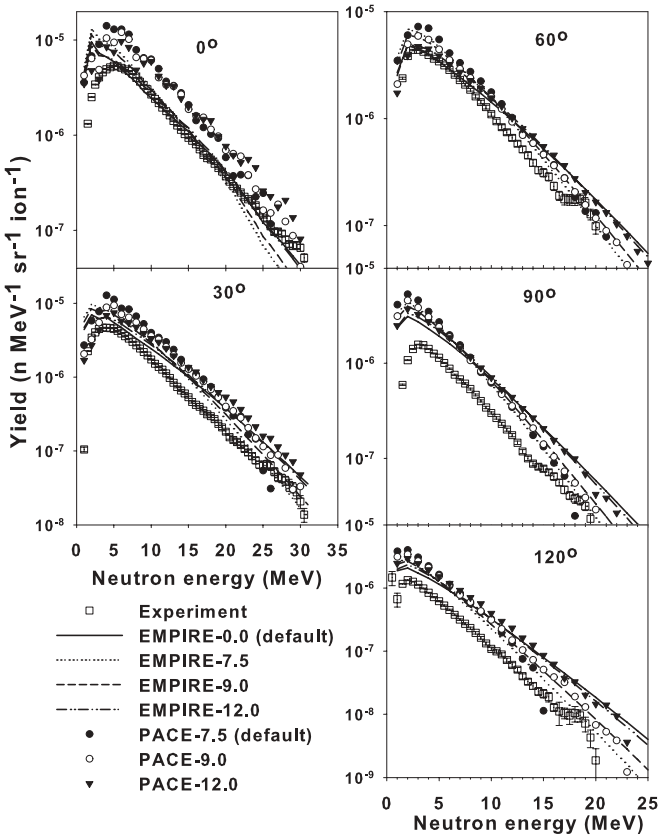

FIG. 8. Calculated energy distributions of neutron yield from 110 MeV ^{19}F on a thick ^{27}Al target at 0°, 30°, 60°, 90°, and 120°. Open squares represent measured (unfolded) data. EMPIRE 2.18 results with different level-density options are plotted (i) as solid lines for EMPIRE-specific dynamic level densities (default option), (ii) as dots for the FGLD with $a = A/7.5$ (MeV^{-1}), (iii) as dash for FGLD with $a = A/9.0$ (MeV^{-1}), (iv) as dash with two dots for FGLD with $a = A/12.0$ (MeV^{-1}). PACE-2 results are plotted (v) as solid circles for FGLD with $a = A/7.5$ (MeV^{-1}) (default option), (vi) as open circles for FGLD with $a = A/9.0$ (MeV^{-1}), and (vii) as solid inverted triangles for FGLD with $a = A/12.0$ (MeV^{-1}).

PACE-2 results with $a = A/12.0$ is closer to the experimentally measured distribution particularly at low energies but overestimate the measured data more than the EMPIRE results. Both EMPIRE and PACE results with $a = A/9.0$ overestimate the experimental data at low emission energies. It is seen that PACE-2 results overestimate the experimental data as well as EMPIRE 2.18 calculations at all values of the a parameter though it gives better results with smaller value of the a parameter.

Similar results of energy differential neutron yield at different angles are plotted in Fig. 8 and we make the same observations as in the case of angle-integrated neutron yield distributions.

The fact that EMPIRE results with Fermi-gas level-density option and $a = A/12.0$ agrees fairly well with the recommended dynamic approach (default) leads us to assume that, based on the present measurement, the value of $a = A/12.0$ is justified. The value of a parameter as given by Ignatyuk and Capote [20] is around 5, which makes approximately $a = A/9.0$. The Fermi-gas level-density parameter does not depend on the excitation energy of the nucleus. The results of all consistent microscopic calculations of the nuclear level-density display damping of the shell effects at high excitation energy and the level-density parameter a tends to an asymptotic value of $\tilde{a}$ at high excitations. Using the formulas suggested by Ignatyuk and Capote [20] as

$$\tilde{a} = \alpha A + \beta A^2 \tag{11}$$

with $\alpha = 0.1125$ and $\beta = 1.22 \times 10^{-4}$ we get the value of $\tilde{a} = 4.669$ that approximately corresponds to $A/10.0$. Because we do not observe very significant differences between the calculated results with $a = A/9.0$ and $a = A/12.0$, we can recommend the value of the a parameter can be anything between these two values.

A. Angular distribution

As can be seen from Fig. 3 the EMPIRE results match the energy distribution at 0° except at very low energies.

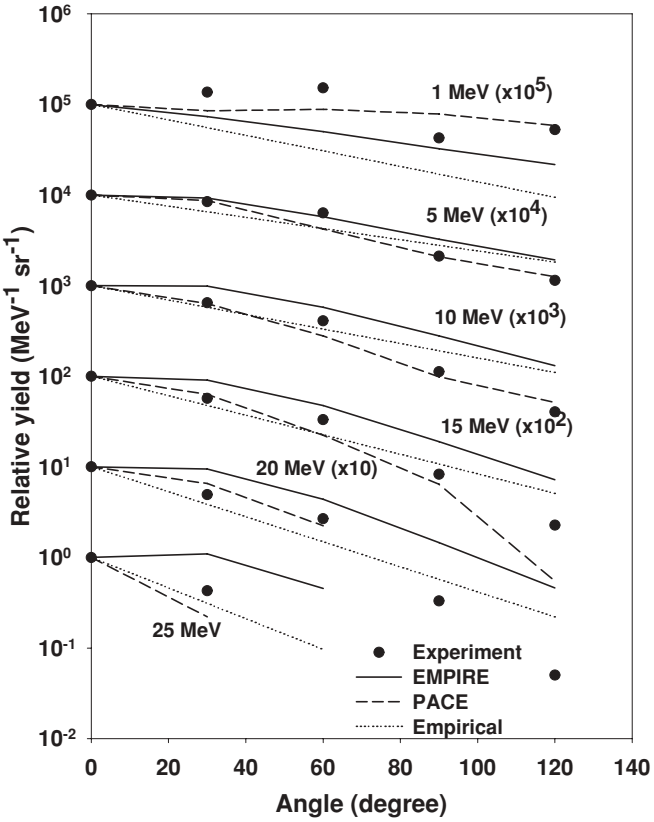

FIG. 9. Relative angular distributions of emitted neutrons from 110 MeV ^{19}F on thick ^{27}Al target at different emission energies in the laboratory system. The data at each emission energy are normalized to emissions at 0°. The symbols are experimental data (unfolded), the solid lines are the results from EMPIRE 2.18, the long dashes are the results from PACE-2, and the dash-dots are results from the empirical relation suggested by Maity *et al.* [21]. For experimental data, the angles of acceptance of the detector are ±0.96° for 0°–90° and ±1.43° for 120°.

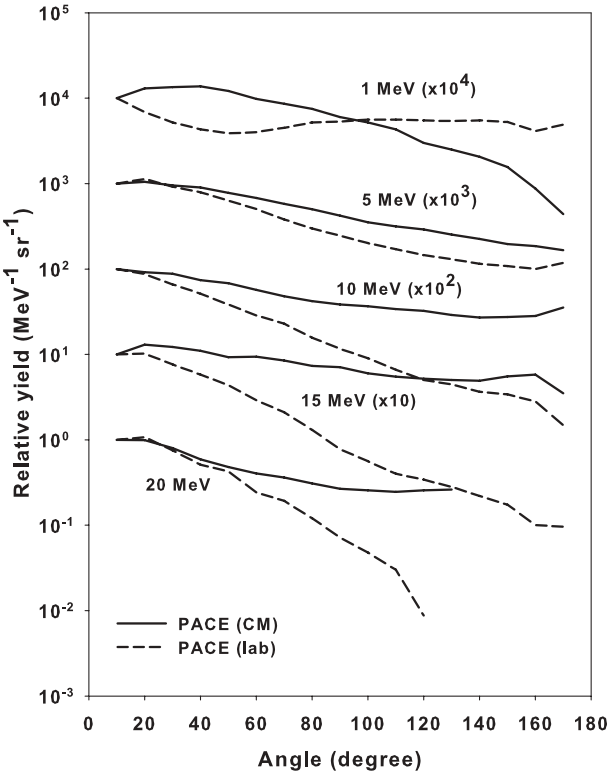

FIG. 10. Relative angular distributions of neutron emission cross sections from ^{19}F + ^{27}Al reaction at 110 MeV at different emission energies. The calculated data using PACE-2 at each emission energy are normalized to emission cross section at 0°. The solid lines are the converted data in the center-of-mass system and the long dashes are the data in the laboratory system as given by PACE-2.

With increasing angle, particularly at 90° and 120°, EMPIRE 2.18 overpredicts the measured data to a great extent. It is evident that the calculated angular distribution is flatter compared to the experimental observation. Consequently, we may conclude that the assumption that neutron emission in the center-of-mass system is isotropic may not be valid. PACE-2, however, overpredicts the experimental energy distribution at all angles by almost the same factor. Except for this factor of overprediction, the decreasing trend with increasing angle of emission is better reproduced by PACE-2 results.

Maiti *et al.* [21] studied the angular distribution of neutrons emitted from thick targets due to heavy-ion-induced reactions and arrived at an empirical relation based on the analysis of a few available experimental data. This empirical relation is essentially an exponential function of the emission angle and can be described as a function of the energy differential neutron yield $Y(\epsilon)$

$$Y(\epsilon,\theta) = \frac{Y(\epsilon)}{4\pi}\frac{m}{1-\exp(-90m)}\exp(4.47 - m\theta), \qquad (12)$$

where θ is in degrees and ϵ in MeV. The parameter m is given as

$$m = p\left(\frac{\epsilon}{E}\right) + q\left(\frac{\epsilon}{E}\right)^{-1}, \qquad (13)$$

where E is the incident projectile energy and

$$p = 0.3898 - 0.4028\sqrt{x}\exp(0.4277x) \qquad (14)$$

$$q = 3.9976 \times 10^{-4} - 0.0306\exp\left(\frac{4.9164 - x}{1.2684}\right) \qquad (15)$$

with $x = E/A_c$, A_c being the mass of the target + projectile composite system.

To visualize the trend in angular distribution of emitted neutrons, we plotted in Fig. 9 the angular distribution at different neutron emission energies. For each plot the data are normalized at 0° for each emission energy. Figure 9 reveals that PACE-2 results (long dash) approximate the trend of experimental angular distribution more closely compared to the EMPIRE 2.18 results (solid lines). The empirical expression given by Maiti *et al.* (dotted) fits the trend broadly and can be considered as a representation of the average angular distribution.

To have an idea how the angular distributions are in the center-of-mass system, we converted to the center-of-mass system the angular distribution of emitted neutrons predicted by PACE-2 in the laboratory system. The resultant plot is

shown in Fig. 10 along with the angular distribution in the laboratory. In this case the data shown are not thick target neutron yield but neutron emission cross sections at 110 MeV for ^{19}F on ^{27}Al normalized to unity at 0°. The converted data were smoothed to smear out statistical fluctuations. It can be observed that the angular distributions at different emission energies in the center of mass, although not as forward peaked as in the laboratory system, cannot be considered as isotropic in nature. Such a trend is not unexpected because of the large angular momentum brought in by the projectile and consequent spin alignment of the composite system, as mentioned in the Introduction. However, in some nuclear reaction model code calculations (e.g., EMPIRE), compound nuclear emissions from heavy-ion-induced reactions are considered to be isotropic in the center-of-mass system. Additionally, in Fig. 10 the angular distribution in the center of mass shows an upward trend at large angles. Such a trend has been reported by Simon and Ahrens [22], who interpreted this to be a result of the transfer of part of the projectile ion to the target nucleus, which moves backward in the center-of-mass system.

VI. CONCLUSION

We reported in this article measurement and analysis of thick target neutron yield distributions at different emission angles from the $^{19}\mathrm{F} + {}^{27}\mathrm{Al}$ reaction at 110 MeV. The energy distributions suggest emissions from an equilibrated system that can be adequately predicted by the Hauser-Feshbach theory. Analysis of the reaction (fusion) cross section, level-density parameters, and optical model parameters were done using the present experimental data and within the framework of two reaction model codes, EMPIRE 2.18 and PACE-2. The reaction cross sections are predicted closer to earlier reported experimental data by the Bass model compared to the results of the coupled-channels calculations. The dynamic approach in the level-density option as used in EMPIRE 2.18 gives a good fit to the measured data. When the Fermi-gas level-density option is used, the parameter $a = A/12.0$ MeV^{-1} gives an equally good fit to the present experimental data. It is also observed from the analysis of the angular distribution of emitted neutrons that the emissions in the center-of-mass system are not isotropic, which is expected as discussed earlier.

[1] L. Heilbronn, T. Nakamura, Y. Iwata, T. Kurosawa, H. Iwase, and L. W. Townsend, Rad. Prot. Dosim. **116**, 140 (2005).
[2] D. Dhar, S. N. Roy, T. Bandyopadhyay, and P. K. Sarkar, Phys. Rev. C **67**, 024607 (2003).
[3] P. K. Sarkar, T. Bandyopadhyay, G. Muthukrishnan, and S. Ghosh, Phys. Rev. C **43**, 1855 (1991).
[4] T. Kato and T. Nakamura, Nucl. Instrum. Methods Phys. Res. A **311**, 548 (1992).
[5] T. Nakamura and Y. Uwamino, Phys. Rev. C **29**, 1317 (1984).
[6] E. L. Hubbard, R. M. Main, and R. V. Pyle, Phys. Rev. **118**, 507 (1960).
[7] K. Shin, K. Miyahara, E. Tanabe, and Y. Uwamino, Nucl. Sci. Eng. **120**, 40 (1995).
[8] M. Nandy, T. Bandyopadhyay, and P. K. Sarkar, Phys. Rev. C **63**, 034610 (2001).
[9] C. Sunil, A. Saxena, R. K. Choudhury, and L. M. Pant, Nucl. Instrum. Methods Phys. Res. A **534**, 518 (2004).
[10] M. Maity, S. N. Roy, M. Nandy, and P. K. Sarkar, Phys. Rev. C **71**, 034601 (2005).
[11] D. Dhar, S. N. Roy, M. Nandy, and P. K. Sarkar, Phys. Rev. C **67**, 064611 (2003).
[12] M. Herman, R. Capote, B. V. Carlson, P. Oblozinsky, M. Sin, A. Trkov, H. Wienke, and V. Zerkin, Nucl. Data Sheets **108**, 2655 (2007).
[13] A. Gavron, Phys. Rev. C **21**, 230 (1980).
[14] S. Marrone *et al.*, Nucl. Instrum. Methods Phys. Res. A **490**, 299 (2002).
[15] M. Matzke, Rad. Prot. Dosim. **107**, 155 (2003).
[16] C. Sunil, M. Maiti, M. Nandy, and P. K. Sarkar, Radiat. Prot. Dosim. **123**, 277 (2007).
[17] J. F. Ziegler, J. P. Biersack, and U. Littmark, *The Stopping and Range of Ions in Solids* (Pergamon Press, New York, 1985).
[18] R. Bass, Phys. Rev. Lett. **39**, 265 (1977).
[19] M. S. Chiou, M. W. Wu, N. Easwar, and J. V. Maher, Phys. Rev. C **24**, 2507 (1981); P. Frobrich, Phys. Rep. **116**, 337 (1984).
[20] A. V. Ignatuk and R. Capote, International Atomic Energy Agency, Vienna, Report No. IAEA-TECDOC-1506, "Handbook for calculations of nuclear reaction data, RIPL-2" (2006).
[21] M. Maity, M. Nandy, S. N. Roy, and P. K. Sarkar, Nucl. Instrum. Methods Phys. Res. A **556**, 577 (2006).
[22] W. G. Simon and S. T. Ahrens, Phys. Rev. C **2**, 1292 (1970).